Deep Learning for Resolving 3D Microstructural Changes in the Fibrotic Liver

William M. Laprade[1,2,9], Behnaz Pirzamanebin[2,3,9], Rajmund Mokso[2,4], Julia Nilsson[5,6], Vedrana A. Dahl[1,2], Anders B. Dahl[1,2], Dan Holmberg[6,7,8], and Anja Schmidt-Christensen[6,8]

[1] Department of Applied Mathematics and Computer Science, Technical University of Denmark, Kgs. Lyngby, Denmark,
willap@dtu.dk
[2] Quantification of Imaging Data from MAX IV, DTU, Denmark
[3] Department of Statistics, Lund University, Lund, Sweden
behnaz.pirzamanbein@stat.lu.se
[4] Department of Physics, Technical University of Denmark, Kgs. Lyngby, Denmark
[5] Laboratory Medicine, University of California, San Francisco, San Francisco, USA
[6] Department of Experimental Medical Sciences, Lund University, Malmö, Sweden
[7] Department of Medical Biosciences, Umeå University, Umeå, Sweden,
[8] Lund University Diabetes Center, Lund University, Malmö, Sweden
[9] these authors contributed equally to this work

Abstract. Portal hypertension, a life-threatening complication of cirrhosis, is largely triggered by increased intrahepatic vascular resistance. Fibrosis, regenerative nodule formation, intrahepatic angiogenisis and sinusoidal remodelling are classical mechanisms that account for increased intrahepatic vascular resistance in cirrhosis. Our study leverages high-resolution 3D synchrotron radiation-based microtomography and a deep learning-based segmentation approach to investigate these microstructural changes in the liver. By employing a multi-planar U-Net model, trained using annotated tomographic slices sourced from our developed online learning tool, we effectively quantify critical vascular parameters such as sinusoid proportions, local thickness, and connectivity. These insights advance our understanding of liver microarchitecture and also allows correlating vascular parameters to inflammation and fibrosis severity. Understanding and quantifying these microstructural changes is essential to be able to predict the transition from seemingly benign conditions like steatosis or mild inflammation to severe fibrosis and cirrhosis.

Keywords: Browser-based segmentation tool · 3D synchrotron x-ray microtomography · Liver sinusoidal network

1 Introduction

Liver disease is a significant global health burden, causing over two million deaths annually. Advanced fibrosis, a critical phase of liver disease, substantially increases mortality risk and is closely linked with a fourfold increase in cardio-

vascular events [5]. Nearly 90% of individuals diagnosed with cirrhosis eventually develop portal hypertension, primarily due to increased vascular resistance within the liver [9]. This resistance is partly attributed to the remodeling of sinusoids by hepatic stellate cells, which create a stiff, collagen-rich matrix characteristic of fibrosis [19,21]. Despite significant progress in understanding liver fibrosis at the molecular level, translating this knowledge into clinical practice has been challenging. A comprehensive understanding of the evolving pathological changes and detailed anatomical data on vascular and cellular adaptations remains elusive.

Traditional 2D histological methods are inadequate for capturing the complex quantitative nuances of cellular and tissue architecture, necessitating advanced large-field, high-resolution 3D imaging techniques. To address this challenges, we employed the NIF mouse model that spontaneously develops chronic liver inflammation and fibrosis [6,7,18], combined with Synchrotron Radiation x-ray micro-Computed Tomography (SRµCT). SRµCT technique provides superior image quality and submicron resolution [22], allowing us to explore 3D microstructural changes during fibrosis progression. The technique has proven its efficacy in 3D visualization, capturing hepatic proliferative bile ductules [13] microvascular alterations at the sinusoidal and capillary scale [27,28], and distinguishing pathological tissues [17].

Our study introduces a novel analysis pipeline for liver fibrosis analysis using deep learning with high-resolution SRµCT, significantly enhancing the visualization and quantification of fibrotic changes.

High-resolution imaging: Our SRµCT images surpass previous works in quality, providing higher cellular resolution that makes inflammatory cells in the liver visible which has previously not been done using µCT. This capability allows us to quantify the 3D structural differences between lesion and unaffected regions in the same scan and enables the visibility of smaller, more complex structures within the liver – structures that were unresolvable in previous works [27].

Segmentation tool: We have developed a browser-based annotation tool [10] that utilizes deep learning [23] to facilitate efficient data labeling and image segmentation, with necessary overlays to allow visual inspection and ensure segmentation quality [23]. The tool utilizes a 2D multi-planar U-Net for image segmentation, chosen for its faster training speed over a typical 3D U-Net, in order to get quick feedback during use. U-Net and its many variants (e.g. [12,29]) are widely used for the segmentation of biological data [4,24]. It has become a standard in microscopy image segmentation as well, where it has been applied to tasks such as 3D organelle segmentation [10] and synaptic cleft segmentation [11], among others [2]. Specifically, the multi-planar U-Net [20] has also previously been shown to be effective for microscopy segmentation with small, sparsely annotated datasets [15].

Quantitative 3D analysis: Unlike previous studies that focused on larger vessels or used simple thresholding techniques for microvasculature analysis, our method quantifies the 3D structure of fibrotic lesions. We measure lesion size

[10] https://github.com/laprade117/interactive-unet

and assess adaptive changes in the sinusoid network following injury and fibrosis, providing a detailed understanding of the microstructural disruptions [15][20].

We segment the SRμCT scans into distinct volumes, differentiating between sinusoid and non-sinusoidal, vessel and non-vessel, and lesion and unaffected regions. We then visually and quantitatively analyze disrupted sinusoidal networks and vascular complexities in fibrotic livers, demonstrating significant changes that potentially contribute to sinusoidal hypertension and liver damage (Fig. 1). Our study addresses the significant gaps in current liver fibrosis research but also introduces innovative tools and methodological pipelines that enhance the understanding and management of this severe condition.

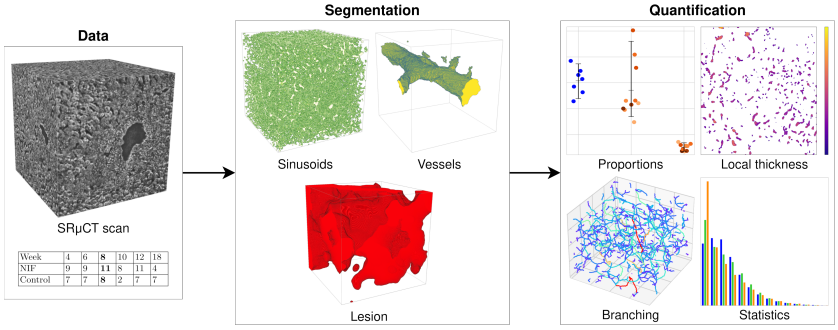

Fig. 1. An overview of our analysis pipeline. We segment our SRμCT scans into three segmentation volumes: sinusoid and non-sinusoid, vessel and non-vessel, and lesion and unaffected regions. We then combine the segmentation volumes and compute quantification measures and statistics. The table in the data block describes the number of scans we have of both NIF and control at different stages of disease. Bold indicates the scans that we investigate in detail in this paper.

2 Data

Mice livers were perfused with PBS via the inferior vena cava, formalin-fixed and paraffin-embedded [7]. 36 tissue blocks, from 4- to 18-weeks old NIF (fibrosis induced) and control mice, were scanned at 2 to 3 randomly selected regions, for a total of 87 image volumes. We include a table in the data block of Fig. 1 for an overview of the collected scans. Following SRμCT image acquisition, liver tissue was sectioned and stained with Hematoxylen & Eosin (H&E) and Picro-Sirius Red (PSR) [7] to differentiate tissue structures and compare with their corresponding synchrotron images. We use all 87 volumes for segmentation, and perform an in-depth quantification of the 8-week (8w) NIF (n=11) and control mice (n=8) volumes. After segmentation, we discard 1 NIF and 1 control from the quantification due to large vessels occupying the volumes leaving little information about cellular structure.

3 Image processing

3.1 Preprocessing

Before training the segmentation models, a series of preprocessing steps were implemented to normalize for imaging variance and artifacts (Fig. 2). To preserve memory, and increase processing speed, a center crop is applied to remove border artifacts followed by 2× binning to achieve a final shape of $(800 \times 800 \times 800)$ with a resolution of 0.65 µm per voxel (Fig. 2a). The bias field is removed by fitting a linear regression model to the pixels in the image and subtracting the resulting prediction. Bright artifacts surrounding the vessels are removed by masking the volumes with a high threshold value, smoothing the mask using a Gaussian filter, and then subtracting it from the original volume (Fig. 2b). Finally, all volumes are mean standardized and squeezed down to the 0-1 range (Fig. 2c,d).

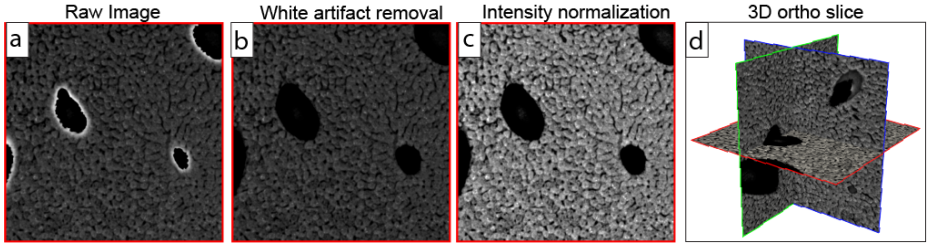

Fig. 2. Data pre-processing steps. 2D presentation of RAW images (a), bias and white artifact corrected (b), final intensity normalized images (c), and ortho-view of pre-processed image stack (d).

3.2 Segmentation

Architecture For segmentation, we use a standard 2D U-Net trained in a multi-planar fashion by utilizing training samples extracted at random positions and orientations. At inference time, the 2D model predicts along the 3 primary axes and averages the results together for a final 3D prediction in a multi-planar fashion [20].

Browser-based segmentation tool: To facilitate efficient annotation and model training, we utilized an online learning tool that we developed to annotate volumes efficiently. The tool is a simple user interface that displays a randomly oriented and positioned slice to the user. The user then annotates the slice using a paint brush tool before moving on to another slice. At any point a model can be trained within the interface and the resulting predictions can be overlayed on the current slice to guide the user during the annotation process. A weight map is used to ensure that the models are trained only on the pixels that the user annotates, allowing quick sparse annotations to be made in each

slice. Once satisfied with the trained model, the user can then use the model to segment the entire volume.

The models are trained using the Adam optimizer with the batch size and learning rate chosen within the tool. During most runs, best results are obtained with batch sizes of 1, 2, and 4 with learning rates 0.001 and 0.0001. To account for any possible class imbalance introduced by the user during the annotation process, a loss function based on Matthew's correlation coefficient [1,3] (MCC) with a second binary cross-entropy (BCE) term is used to provide smoother gradients. The loss is computed via,

$$\mathrm{MCC} = \frac{(\mathrm{TP} \cdot \mathrm{TN}) - (\mathrm{FP} \cdot \mathrm{FN})}{\sqrt{(\mathrm{TP} + \mathrm{FP})(\mathrm{TP} + \mathrm{FN})(\mathrm{TN} + \mathrm{FP})(\mathrm{TN} + \mathrm{FN})}}$$

$$\mathrm{BCE} = -\frac{1}{N}\sum_{i=0}^{N} y_i \log(\hat{y_i}) + (1 - y_i)(1 - \log(\hat{y_i}))$$

$$L = \mathrm{MCC} + \mathrm{CE}$$

and averaged over each class. In the MCC loss, the true positive (TP), true negative (TN), false positive (FP), and false negative (FN) counts are normalized by the number of annotated pixels, and non-annotated pixels are ignored. The MCC function is bounded between -1 and 1 with 1 being a perfect score, 0 being random guessing and -1 being perfectly incorrect.

Segmentation process: During annotation, 2-4 volumes are selected and the interactive segmentation tool is used to annotate slices from these volumes and train a segmentation model. The model is then used to fully segment those 2-4 volumes. This is repeated on small groups of volumes to both expedite the process and enhance segmentation by leveraging knowledge across more than one volume. A final model is then trained on 40 segmented volumes and used to segment the entire dataset of 80 volumes. Two models are built during this process, one for segmentation of the lesion and unaffected regions and one for segmentation of vessels/sinusoids.

3.3 Postprocessing

Lesion segmentations: To eliminate line artifacts generated by the multi-view segmentation, Gaussian filtering was applied, followed by a binary dilation. This produces a smooth segmentation that outlines the lesion regions in the volume (Fig. 3a-d).

Vessel/sinusoid segmentations: Line artifacts are eliminated via Gaussian smoothing at a low sigma. Given that the sinusoidal diameters range from 7 µm in the periportal and 15 µm in the pericentral area [25,26,28], connected components were applied to remove all disconnected objects that could fit into a sphere with a diameter of 6 µm (Fig. 3e-h). Vessels and sinusoids are separated into two separate masks by viewing the volume from 9 different views. In each view, the area of the object to which the pixel belongs is calculated, and if it

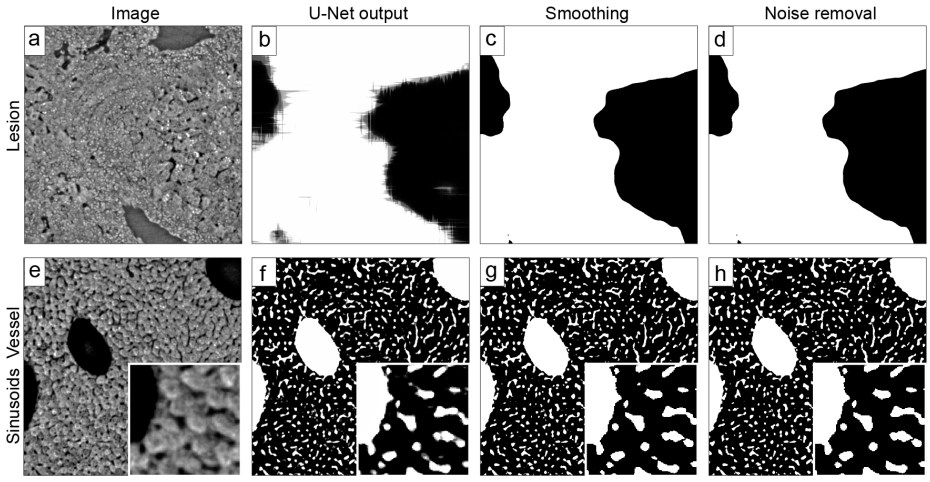

Fig. 3. High-quality structural predictions from NIF (a-d) and control (e-h) liver volumes. (a,e) 2D tomographic slice (input image) and predictions for lesions (b-d) or vasular structures (f-h). U-net raw predictions (b,f) were postprocessed by smoothing (c,g) and noise removal (d,h).

exceeds a specified area threshold, it is designated as a vessel; otherwise, it is assigned a sinusoid label. The final decision on whether the pixel is a vessel or a sinusoid is determined through majority voting.

3.4 Quantification

Proportions: To assess adaptive changes in the sinusoidal network following injury and fibrosis, changes in the sinusoidal network were quantified within control and both lesion and unaffected regions of NIF livers. The proportion of sinusoids in control mice is determined by dividing the number of sinusoid voxels by the total volume, excluding vessels.

To quantify the proportion of sinusoidal volume in NIF mice within lesion regions, the volume of sinusoids within the lesion regions is compared to the total volume of the lesions themselves. A similar approach is applied in unaffected regions.

Local thickness: The local thickness is computed as, for each voxel within a 3D object, it is assigned the radius of the largest sphere that can fit entirely within the object while encompassing the voxel [8].

Branching: The branch analysis is used to measure the connectivity and length of the sinusoidal network. First, the segmented sinusoid is transformed into a continuous skeleton [16], then a graph-based technique is employed [14] to identify the branches within the skeleton. Branch types were categorized into three types: T_0 for endpoint-to-endpoint branches (isolated branch), T_1 for junction-to-endpoint branches, and T_2 for junction-to-junction branches. Since the types

refer to branches, not nodes, it is assumed that each T_0 branch has 2 nodes, T_1 has 1 node, and T_2 has 1 node, plus one additional node for the entire branch it belongs to. To calculate the degree of connectivity, the count of T_2 nodes, increased by one for each branch, is divided by the sum of the T_1 and twice the T_0 nodes. This approach aids in understanding of the overall connectivity within the sinusoidal network, with values close to zero indicating lower connectivity.
Statistical Test: The Mann–Whitney U test, a non-parametric test, is employed to compare the differences in means between the control and NIF mice, as well as between lesion and unaffected regions.

4 Results and Discussion

Detection of local structure-specific alterations in the fibrotic liver: SRμCT can identify microstructural changes in the development of liver fibrosis while preserving the volumetric architecture (Fig. 4). Employing deep learning guided by correlative histology, structural features like lesions, vessels, and sinusoids were segmented. Lesions, characterized by persistent inflammation and fibrosis, were confirmed through validation using consecutive histological sections stained with H&E (Fig. 4a,b) and Picrosirius Red (Fig. 4o,p).

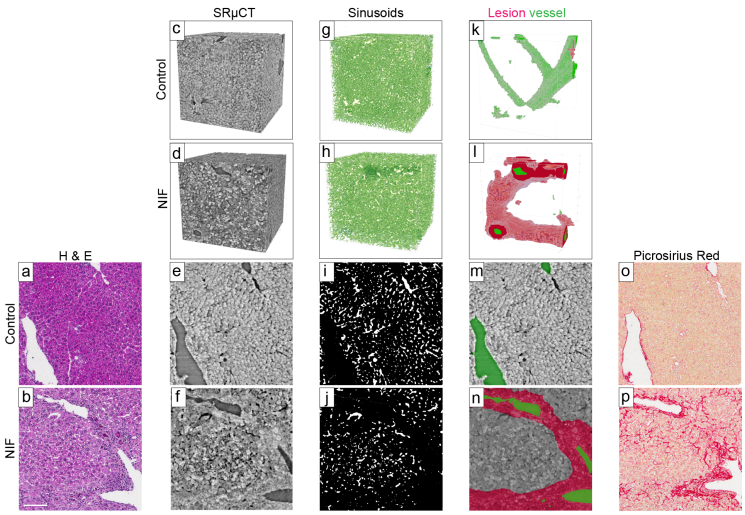

Fig. 4. SRμCT reveals microvascular changes in liver lesions of NIF mice. Representative SRμCT scans of control and fibrotic NIF livers (c-f), with 3D segmented features (g-n). Histological sections, stained with H&E (a,b) or PSR (o,p) matched with x-ray slices (e,f), segmented sinusoid (i,j), and lesion and vessel features (m,n).

Remodulation of the sinusoidal network: To assess adaptive consequences in the sinusoidal network resulting from injury and fibrosis, we measured lesion

size and quantified sinusoidal parameters for NIF lesion regions, NIF unaffected regions, and control volumes. Significantly decreased sinusoid proportions were observed in NIF lesions compared to healthy controls (p-value = 0.0063) and unaffected NIF regions (p-value = 0.00001) (Fig. 5d). When comparing the mean local thickness of both sinusoidal and non-sinusoidal structures within the liver volumes, it becomes evident that the control volumes show a tight clustering, indicating minimal variation in local thickness. Conversely, the NIF lesions display a broader spread, implying a lower vascular density in 8w NIF lesions (Fig. 5a-c). The examination of microvascular changes in liver fibrosis can provide insights

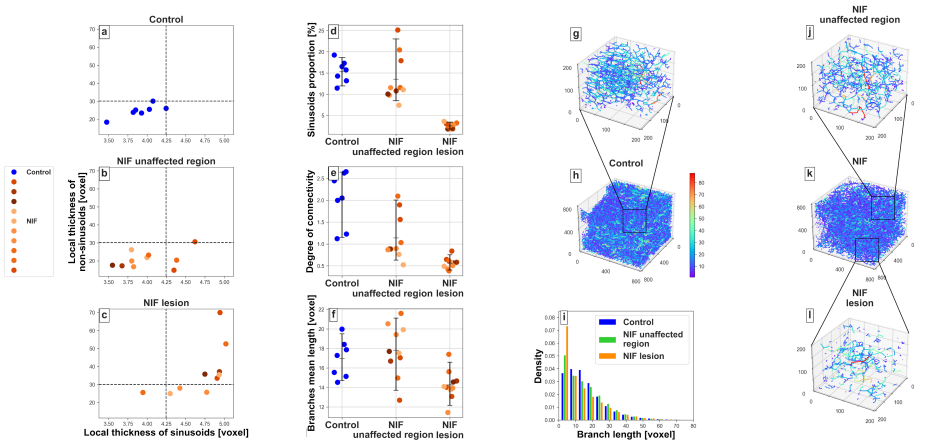

Fig. 5. Fibrotic lesions show disrupted sinusoidal organization and decreased vascular complexity. (a-c) sinusoid network density expressed as local sinusoid thickness against non-sinusoids, (d) Sinusoid volume proportions, (e) degree of sinusoid connectivity, (f) mean branch length per volume, and (i) histogram of branch length. Colour codes in NIF represent measures from the same NIF scan, lesion vs. unaffected regions. Branching of sinusoidal network in control (g,h) and NIF mice (j-l), displayed as entire network (h,k) or detailed zoomed-in illustrations (g,j,l). The color range indicates branch length.

into the mechanisms behind the resistance to blood flow and the direct increase in portal pressure. Here, we utilize the 3D structure of liver sinusoids to quantify vascular branching geometric features in fibrotic livers in more detail (Fig. 5e-l). We found that fibrosis affected the microcirculation in the liver characterized by a disrupted sinusoidal network with reduced connectivity (Fig. 5e) and reduced mean branch length (Fig. 5f,i) compared to healthy controls.

5 Conclusion

Leveraging high quality SRμCT scans and our interactive segmentation and quantification workflow, our study achieved precise and rapid localization of

diverse structural features within intact liver tissue. Our 3D analysis, which includes local thickness, connectivity, and branch length, uncovered significant differences between fibrotic lesions and unaffected regions. Notably, the remodulation of microvasculature in fibrotic liver regions, characterized by increased local sinusoid thickness, decreased total sinusoid volume, and a fragmented vascular network, as evidenced by our measurements, suggest a potential mechanism for decreased blood flow and impaired liver function. This study highlights the advanced capabilities of high-resolution SRμCT imaging in detecting detailed microstructural changes but also underscores the effectiveness of our deep learning-based approach in enhancing the quantification and understanding of liver fibrosis progression.

Prospect of application: Our interactive segmentation tool, is broadly applicable and simple enough to use that clinicians and medical researchers without strong machine learning knowledge can use it effectively. Additionally, the analysis pipeline used here can be applied in future studies for understanding the microvascular and structural changes in other organs and diseases.

References

1. Abhishek, K., Hamarneh, G.: Matthews correlation coefficient loss for deep convolutional networks: Application to skin lesion segmentation. In: 2021 IEEE 18th International Symposium on Biomedical Imaging (ISBI). IEEE (2021)
2. Aswath, A., Alsahaf, A., Giepmans, B.N., Azzopardi, G.: Segmentation in large-scale cellular electron microscopy with deep learning: A literature survey. Medical Image Analysis **89**, 102920 (2023)
3. Chicco, D., Jurman, G.: The advantages of the matthews correlation coefficient (mcc) over f1 score and accuracy in binary classification evaluation. BMC Genomics **21**(1) (2020)
4. Du, G., Cao, X., Liang, J., Chen, X., Zhan, Y.: Medical image segmentation based on u-net: A review. Journal of Imaging Science and Technology **64**(2), 020508–1–020508–12 (2020)
5. Ekstedt, M., Hagström, H., Nasr, P., Fredrikson, M., Stål, P., Kechagias, S., Hultcrantz, R.: Fibrosis stage is the strongest predictor for disease-specific mortality in nafld after up to 33 years of follow-up. Hepatology **61**(5), 1547–1554 (2015)
6. Fransén Pettersson, N., Deronic, A., Nilsson, J., Hannibal, T.D., Hansen, L., Schmidt-Christensen, A., Ivars, F., Holmberg, D.: The immunomodulatory quinoline-3-carboxamide paquinimod reverses established fibrosis in a novel mouse model for liver fibrosis. PLOS ONE **13**(9), e0203228 (2018)
7. Fransén-Pettersson, N., Duarte, N., Nilsson, J., Lundholm, M., Mayans, S., Larefalk, A., Hannibal, T.D., Hansen, L., Schmidt-Christensen, A., Ivars, F., Cardell, S., Palmqvist, R., Rozell, B., Holmberg, D.: A new mouse model that spontaneously develops chronic liver inflammation and fibrosis. PLOS ONE **11**(7), e0159850 (2016)
8. Gostick, J., Khan, Z., Tranter, T., Kok, M., Agnaou, M., Sadeghi, M., Jervis, R.: Porespy: A python toolkit for quantitative analysis of porous media images. Journal of Open Source Software **4**(37), 1296 (2019)
9. Groszmann, R.J., Abraldes, J.G.: Portal hypertension: From bedside to bench. Journal of Clinical Gastroenterology **39**(4), S125–S130 (2005)

10. Heinrich, L., Bennett, D., Ackerman, D., Park, W., Bogovic, J., Eckstein, N., Petruncio, A., Clements, J., Pang, S., Xu, C.S., Funke, J., Korff, W., Hess, H.F., Lippincott-Schwartz, J., Saalfeld, S., Weigel, A.V., Ali, R., Arruda, R., Bahtra, R., Nguyen, D.: Whole-cell organelle segmentation in volume electron microscopy. Nature **599**(7883), 141–146 (2021)
11. Heinrich, L., Funke, J., Pape, C., Nunez-Iglesias, J., Saalfeld, S.: Synaptic Cleft Segmentation in Non-isotropic Volume Electron Microscopy of the Complete Drosophila Brain, p. 317–325. Springer International Publishing (2018)
12. Isensee, F., Jaeger, P.F., Kohl, S.A.A., Petersen, J., Maier-Hein, K.H.: nnu-net: a self-configuring method for deep learning-based biomedical image segmentation. Nature Methods **18**(2), 203–211 (2020)
13. Keegan, A., Martini, R., Batey, R.: Ethanol-related liver injury in the rat: a model of steatosis, inflammation and pericentral fibrosis. Journal of Hepatology **23**(5), 591–600 (1995)
14. Kollmannsberger, P., Kerschnitzki, M., Repp, F., Wagermaier, W., Weinkamer, R., Fratzl, P.: The small world of osteocytes: connectomics of the lacuno-canalicular network in bone. New Journal of Physics **19**(7), 073019 (2017)
15. Laprade, W.M., Perslev, M., Sporring, J.: How Few Annotations are Needed for Segmentation Using a Multi-planar U-Net?, p. 209–216. Springer International Publishing (2021)
16. Lee, T., Kashyap, R., Chu, C.: Building skeleton models via 3-d medial surface axis thinning algorithms. CVGIP: Graphical Models and Image Processing **56**(6), 462–478 (1994)
17. Lettmann, K.A., Hardtke-Wolenski, M.: The importance of liver microcirculation in promoting autoimmune hepatitis via maintaining an inflammatory cytokine milieu – a mathematical model study. Journal of Theoretical Biology **348**, 33–46 (2014)
18. Nilsson, J., Hörnberg, M., Schmidt-Christensen, A., Linde, K., Nilsson, M., Carlus, M., Erttmann, S.F., Mayans, S., Holmberg, D.: Nkt cells promote both type 1 and type 2 inflammatory responses in a mouse model of liver fibrosis. Scientific Reports **10**(1) (2020)
19. Onori, P., Morini, S., Franchitto, A., Sferra, R., Alvaro, D., Gaudio, E.: Hepatic microvascular features in experimental cirrhosis: a structural and morphometrical study in ccl4-treated rats. Journal of Hepatology **33**(4), 555–563 (2000)
20. Perslev, M., Dam, E.B., Pai, A., Igel, C.: One Network to Segment Them All: A General, Lightweight System for Accurate 3D Medical Image Segmentation, p. 30–38. Springer International Publishing (2019)
21. Poisson, J., Lemoinne, S., Boulanger, C., Durand, F., Moreau, R., Valla, D., Rautou, P.E.: Liver sinusoidal endothelial cells: Physiology and role in liver diseases. Journal of Hepatology **66**(1), 212–227 (2017)
22. Rawson, S.D., Maksimcuka, J., Withers, P.J., Cartmell, S.H.: X-ray computed tomography in life sciences. BMC Biology **18**(1) (2020)
23. Ronneberger, O., Fischer, P., Brox, T.: U-net: Convolutional networks for biomedical image segmentation. In: Medical Image Computing and Computer-Assisted Intervention – MICCAI 2015, p. 234–241. Springer International Publishing (2015)
24. Siddique, N., Paheding, S., Elkin, C.P., Devabhaktuni, V.: U-net and its variants for medical image segmentation: A review of theory and applications. IEEE Access **9**, 82031–82057 (2021)
25. Vollmar, B., Menger, M.D.: The hepatic microcirculation: Mechanistic contributions and therapeutic targets in liver injury and repair. Physiological Reviews **89**(4), 1269–1339 (2009)

26. Wake, K., Sato, T.: "the sinusoid" in the liver: Lessons learned from the original definition by charles sedgwick minot (1900). The Anatomical Record **298**(12), 2071–2080 (2015)
27. W.L., Wagner, S., Föhst, J., Hock, e.a.: 3d analysis of microvasculature in murine liver fibrosis models using synchrotron radiation-based microtomography. Angiogenesis **24**(*), 57–65 (2021)
28. Yoon, Y.J., Chang, S., Kim, O.Y., Kang, B.K., Park, J., Lim, J.H., Yun Huang, J., Kim, Y.K., Byun, J.H., Gho, Y.S.: Three-dimensional imaging of hepatic sinusoids in mice using synchrotron radiation micro-computed tomography. PLoS ONE **8**(7), e68600 (2013)
29. Zhou, Z., Rahman Siddiquee, M.M., Tajbakhsh, N., Liang, J.: UNet++: A Nested U-Net Architecture for Medical Image Segmentation, p. 3–11. Springer International Publishing (2018)